PAPER

Thermally-induced softening of PNIPAm-based nanopillar arrays

Belén Sanz,[a] Catalina von Bilderling,[b] Jimena S. Tuninetti,[c] Lía Pietrasanta,[bd] Carmen Mijangos,[a] Gabriel S. Longo,[c] Omar Azzaroni[c] and Juan M. Giussi*[c]

The surface properties of soft nanostructured hydrogels are crucial in the design of responsive materials that can be used as platforms to create adaptive devices. The lower critical solution temperature (LCST) of thermo-responsive hydrogels such as poly(N-isopropylacrylamide) (PNIPAm) can be modified by introducing a hydrophilic monomer to create a wide range of thermo-responsive micro-/nano-structures in a large temperature range. Using surface initiation atom-transfer radical polymerization in synthesized anodized aluminum oxide templates, we designed, fabricated, and characterized thermo-responsive nanopillars based on PNIPAm hydrogels with tunable mechanical properties by incorporating acrylamide monomers (AAm). In addition to their LCST, the incorporation of a hydrophilic entity in the nanopillars based on PNIPAm has abruptly changed the topological and mechanical properties of our system. To gain an insight into the mechanical properties of the nanostructure, its hydrophilic/hydrophobic behavior and topological characteristics, atomic force microscopy, molecular dynamics simulations and water contact angle studies were combined. When changing the nanopillar composition, a significant and opposite variation was observed in their mechanical properties. As temperature increased above the LCST, the stiffness of PNIPAm nanopillars, as expected, did so too, in contrast to the stiffness of PNIPAm–AAm nanopillars that decreased significantly. The molecular dynamics simulations proposed a local molecular rearrangement in our nanosystems at the LCST. The local aggregation of NIPAm segments near the center of the nanopillars displaced the hydrophilic AAm units towards the surface of the structure leading to contact with the aqueous environment. This behavior was confirmed via contact angle measurements below and above the LCST.

Introduction

Soft nanostructured hydrogel surfaces are increasingly becoming a focus area for both biology and medicine due to their tunable hydration and rigidity features. Hydrogels, which possess a remarkable stimuli-responsive nature, represent one of the most widely used building blocks in adaptive surface creation.[1–4] Engineering such nanostructured surfaces[5] often involves the integration of soft topographic features, such as nanopillars or nanoparticles, into planar substrates in order to control and manipulate the mechanical behavior, adaptability, and functionality of the modified surface.[6] Part of the appeal of these nanostructured systems relies on the strong influence that their physicochemical properties have on cellular and biological interactions. In particular, the influence of hydrogel film mechanical properties on cellular adhesion, migration, proliferation, and growth has attracted significant attention in recent years.[7] For example, Caruso *et al.* reported that tuning the stiffness of thiolated hydrogel films allows mediating cervical cancer cell adhesion.[8]

Among the ample variety of stimuli responsive soft materials, PNIPAm-based hydrogels with triggerable phase transition[9] behavior represent the quintessence of thermo-responsive materials displaying adaptive changes in mechanical properties. In principle, the large change in PNIPAm mechanical properties at the transition temperature is related to the amount of water expelled or absorbed from the hydrogel network. Many thermo-responsive microgels are biocompatible and have been used in several areas, such as scaffolding in tissue engineering, drug delivery, nanomedicine, and cell culture.[10–15]

Crosslinking PNIPAm with other monomers not only controls the mechanical properties of the gel, but also significantly affects the magnitude of the volume transition.[16] For instance, when

[a] *Instituto de Ciencia y Tecnología de Polímeros, CSIC, Juan de la Cierva 3, 28006 Madrid, Spain*

[b] *Instituto de Física de Buenos Aires (IFIBA-CONICET) and Departamento de Física, Facultad de Ciencias Exactas y Naturales, Universidad de Buenos Aires, C1428EHA Buenos Aires, Argentina*

[c] *Instituto de Investigaciones Fisicoquímicas Teóricas y Aplicadas (INIFTA) – Departamento de Química – Facultad de Ciencias Exactas – Universidad Nacional de La Plata – CONICET, 1900 La Plata, Argentina. E-mail: jmgiussi@inifta.unlp.edu.ar*

[d] *Centro de Microscopías Avanzadas, Facultad de Ciencias Exactas y Naturales, Universidad de Buenos Aires, C1428EHA Buenos Aires, Argentina*

cross-linked poly(dimethylsiloxane) (PDMS) is incorporated into a PNIPAm gel, the mechanical toughness of the gel is increased.[17]

The lower critical solution temperature (LCST), phase change kinetics and swelling of NIPAm-based polymers can be controlled through the incorporation of co-monomers that alter the hydrophilic–lipophilic balance of the copolymer, introduce steric hindrance and influence the morphology of the networks formed.[18] Linear PNIPAm homopolymer solutions and PNIPAm gels expel much of their water content and, consequently, their hydrogel properties become significantly altered upon reaching equilibrium after the LCST phase transition.[19] Above a critical concentration and the LCST, they undergo a coil to globule transition resulting in the depletion of solvent and the formation of a compact associative gel network (*i.e.*, gels shrinkage). Several works dealing with the mechanical properties of PNIPAM microgel thin films have reported that the modulus increases monotonically with temperature,[20] and the steepest change occurs near the LCST (∼32 °C), whereas at temperatures well above and below the LCST, the change in the modulus levels off.[21] Hashmi and Dufresne[22] postulated that swollen PNIPAM microgels exhibit Young's moduli of ∼8 kPa at room temperature, but at or above the LCST, these microgels stiffen to ∼86 kPa in the collapsed state.

On the other hand, it has been widely accepted that the incorporation of hydrophilic co-monomers, including acrylic acid (AAc),[23,24] and polymer conjugates such as poly(ethylene glycol) (PEG)[25–28] into PNIPAm systems inhibits complete chain collapse and provides a more porous network, resulting in increased swelling in the gel phase and a decrease in solvent depletion after thermal transition.[29,30] As a result, the integration of hydrophilic monomers into the PNIPAm network decreases its compressive modulus due to the increase in the water content. In this case, water plays a critical part as a plasticizer of the hydrogel network, generating a significant decrease in its mechanical properties, *e.g.*, softening.

The use of PNIPAm microgels as "smart" building blocks with thermo-responsive mechanical properties has been exclusively circumscribed to the creation of soft platforms that stiffen when the environmental temperature is increased above the LCST. In this regard, Pollock and Healy provided an interesting twist to this scenario through different research studies on the dynamic mechanical properties of copolymers of NIPAm and methoxy poly(ethylene glycol) methacrylate (MPEGMA). These authors noticed that the high concentration solutions of these copolymers did not exhibit the expected thermo-mechanical behavior, but instead became softer at higher temperatures as measured by rheometry.[31] Other interesting results were accounted for by Janovák *et al.*[32] who observed that, contrary to expectations, the presence of copolymerized acrylamide (AAm) in a PNIPAm macrogel led to a significant improvement in the mechanical properties. This experimental observation through rheology was ascribed to the strong binding of water molecules *via* hydrogen bonds to the AAm monomers (containing hydrophilic amino groups) resulting in a stronger gel structure.

On the other hand, over the last decade, the use of AAO templates has attracted increasing interest in polymer science, due to the possibility of obtaining polymers with different morphologies, *i.e.*, nanofibers, nanorods, and nanotubes with homo- and co-polymers by polymer infiltration.[33–39] It has also been reported that a polymer confined to nanocavities exhibits different properties from those of the bulk, *i.e.*, differences in the early stages of crystallization.[40,41] Even though extensive literature deals with the use of AAO templates for nanomolding of polymers, powdered or film polymers must be infiltrated in the nanocavities at a high temperature for a relatively long time, from hours to days. Over such a time period, degradation of the polymer chain could occur.[42] Therefore, recent studies have revealed radical polymerization taking place within the cavities of the AAO template.[43–45] Among other advantages, the one-step *in situ* fabrication of polymer nanostructures in the AAO nanocavities overcomes the degradation issues. Chang *et al.* have recently fabricated one-dimensional polymer nanomaterials through microwave energy.[46] Even though the methods described have successfully achieved the objectives, the possibility of combining AAO templates with controlled/"living" radical polymerization techniques leads to more controlled and friendly polymerization systems. Atom transfer radical polymerization (ATRP) and reversible addition–fragmentation chain-transfer polymerization (RAFT) have been used for some monomer systems in AAO templates.[47–56] Cui *et al.*[57] have prepared PNIPAm nanotubes by ATRP polymerization using AAO as a template. The diameter of the nanotubes has been controllable and these nanostructures showed a high flexibility.

The aim of this work is two-fold: design, prepare and characterize nanopillars based on PNIPAm microgels with a tunable LCST through surface initiated-atom transfer radical polymerization (SI-ATRP) on laboratory prepared anodized aluminum oxide (AAO) templates and outline a strategy for tuning the mechanical properties of nanostructures based on PNIPAm micro-/nano-gels. To meet these goals, we combined AAO template synthesis with the SI-ATRP of NIPAm and acrylamide (AAm) monomers in order to attain low aspect ratio unidimensional micro-/nano-gels (nanopillars). Infrared (IR) and Raman spectroscopy were used to determine the chemical composition of the polymers. Scanning electron microscopy confirmed the nanostructures obtained and, through atomic force microscopy (AFM), we evaluated the topology and the mechanical properties of our nanopillars, below and above the LCST. The changes in Young's modulus values suggest a local macromolecular rearrangement during transition that was supported by Molecular Dynamics (MD) simulations. Finally, contact angle measurements were used to confirm the rearrangement and establish the surface hydrophilicity of these materials. The use of AAm as a co-monomer allowed tuning not only the LCST but also the surface mechanical properties and the hydrophilicity of the nanopillars obtained. These results represent an important contribution to many areas, such as tissue engineering, drug delivery, and regenerative medicine, to name a few.

Materials and methods

Materials

N-Isopropylacrylamide (Aldrich, 97%), acrylamide (Fluka, 98%), (3-aminopropyl)triethoxysilane (APTES) (Aldrich 99%),

α-bromoisobutyryl bromide (Aldrich, 98%), N,N'-methylene-bisacrylamide (BIS) (Aldrich, 99%), N,N,N',N',N''-pentamethyl-diethylenetriamine (PMDTA) (Aldrich, 99%), CuCl (Aldrich, 99.999%), $CuCl_2$ (Aldrich, 99%), phosphoric acid (Aldrich, 85 wt% in H_2O), and HCl (Aldrich, 37% in H_2O).

Nanopillar synthesis

Nanopillar preparation. Nanopillars were obtained by the ATRP technique, which allows the polymerization in confinement because the reaction is conducted on the nanoreactor walls. This mechanism enables only the polymerization in a confined regime within the nanoreactor. The complete nanopillar synthesis requires a number of steps, as depicted in Scheme 1. These steps are grafting of the ATRP initiator (silanization and reaction with α-bromoisobutyryl bromide) and the ATRP procedure to obtain the PNIPAm nanopillars. The alumina template was previously modified with 3-aminopropyltrimethoxysilane in ethanol for 1 hour according to previous reports.[57,58] The membrane was cured for 1 h in an oven at 150 °C and then modified with the ATRP initiator, 2-bromoisobutyryl bromide, according to the aforementioned works. In order to tune the LCST to higher values, homo- and co-polymers of NIPAm and AAm were prepared, and the general procedure is explained below.

The aminopropylsilane grafted AAO nanoreactor (previously in a vacuum for 30 min) was immersed in an exhaustively degassed solution which contained 4.70 mmol of amide (NIPAm and AAm) and 0.11 mmol of BIS in a mixture of 2 mL of H_2O and 2 mL of MeOH containing 0.105 mmol of CuCl (this compound was added last after purging with nitrogen, to prevent its oxidation) and 0.502 mmol of PMDTA for 48 hours, at room temperature. After this time the AAO nanoreactor with the nanopillars inside was removed from the reaction medium and intensively washed with water. The samples were stored immersed in degassed water in closed containers before specific treatment for each study.

Hydrogel thin film synthesis. The hydrogel thin films were obtained by surface-initiated atom-transfer radical polymerization from glass as described by Wei[59] and Cui.[57]

The glass was first modified with a solution of 2% v/v of 3-aminopropyltrimethoxysilane in absolute ethanol. The silanization reaction was carried out at 40 °C for 2 hours. After this time, the reaction was terminated by rinsing the glass with ethanol. The glass was then cured in an oven at 150 °C for 2 h. The ATRP initiator, 2-bromoisobutyryl bromide, was then grafted onto the silanized AAO template by dipping the glass in 6 mL of superdry tetrahydrofuran containing dry triethylamine (2%, v/v). Afterwards, at 5 °C, 0.016 mL of 2-bromoisobutyryl bromide was added. Then the reaction was continued at room temperature overnight. After that, the glass was rinsed with ethanol and acetone and dried with nitrogen.

The ATRP procedure over the glass was achieved by immersing the substrate in a degassed solution of 10 mmol of acrylic monomer (*N*-isopropylacrylamide or *N*-isopropylacrylamide + acrylamide) and 0.1 mmol of *N,N*-methylenebisacrylamide in a mixture of 3 mL of H_2O and 3 mL of MeOH containing 0.015 g of CuBr and 0.075 mL of PMDETA for 5 hours. After polymerization, the hydrogel thin films were rinsed with H_2O and then dried with nitrogen. The estimated thickness of hydrogels by ellipsometry was 500 nm.

Chemical and morphological characterization

In order to characterize the polymer nanostructures by different techniques, the samples were subjected to different treatments, depending on the method used. The steps for sample preparation are illustrated in Scheme 2.

Scanning electron microscopy. The AAO templates and all nanopillars obtained were morphologically characterized by scanning electron microscopy (SEM) (Philips XL30). In order to perform the analysis of free nanopillars, the aluminum substrate was treated with a mixture of HCl, $CuCl_2$, and H_2O and the alumina was dissolved in 10% wt H_3PO_4. Previously, in order to support the free nanostructures, a coating was placed over the template; Scheme 2. The samples were lyophilized before the study in order to preserve the morphology.

IR and Raman spectroscopy. The obtained nanopillars were chemically characterized by Infrared and Raman spectroscopy,
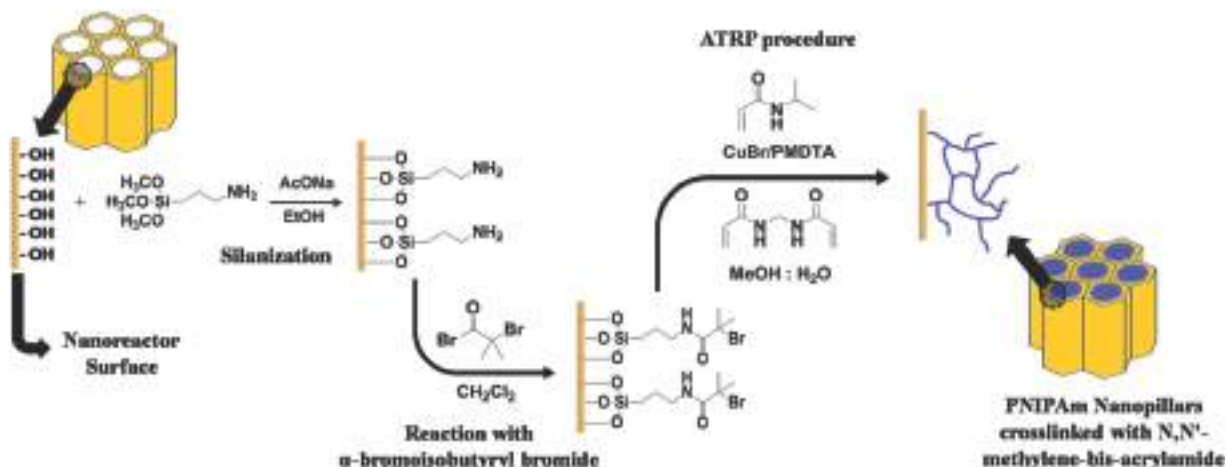
Scheme 1 Steps for the synthesis of PNIPAm nanopillars.
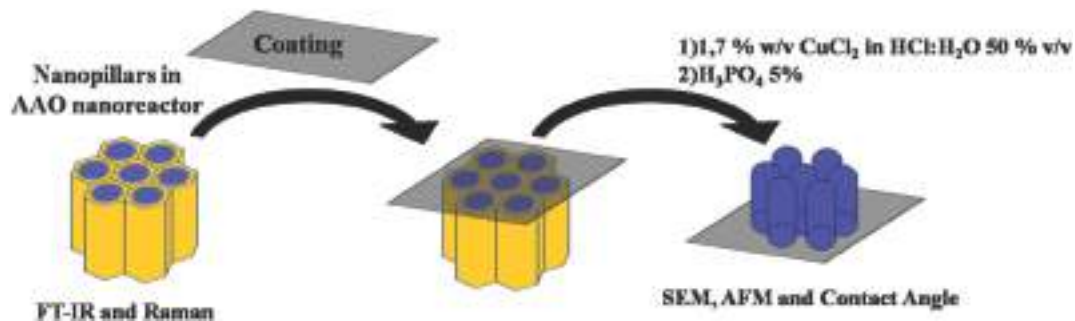
Scheme 2 Sample preparation for each characterization and study. The coating for SEM and AFM was polymethyl methacrylate films.

with a FT-IR Varian 660 and a Renishaw InVia Raman Micro-scope, respectively. The measurements have been carried out with the filled template, that is, the aluminum, alumina and nanopillars inside the nanocavities. ATR experiments were performed to obtain the IR spectra.

The Raman scattering was done by exciting with a 785 nm near-infrared diode laser. A $100\times$, NA090 objective lens was used; giving a laser spot diameter of ~ 1 μm. Data acquisition covered the spectral range 3200–500 cm^{-1} with a spectral resolution of 4 cm^{-1} for each exposure of the CCD detector. Depth profiles were obtained by focusing the microscope stepwise, at 700 nm through the AAO template.

Atomic force microscopy. AFM measurements were performed in aqueous solution (50 mM KCl) using a Multimode 8 AFM (Nanoscope V Controller, Bruker, Santa Barbara, CA). Images were acquired in the peak force tapping mode (PeakForce-Quantitative NanoMechanics, PF-QNM). V-shaped SNML AFM probes (with 0.07 N m^{-1} cantilever nominal spring constant, 20 nm tip radius, and 19° half-open angle of the tip) were used (Bruker). The exact spring constant of the cantilever was determined before each experiment using the thermal tuning method,[60] and the deflection sensitivity was determined in fluid using a Sapphire sample (Bruker) as an infinitely stiff reference material. Force curves were acquired using a PF-QNM AFM, with a maximum applied loading force of 5 nN. From PF-QNM maps, force curves corresponding to nanopillar surfaces were selected to perform quantitative analysis. The contact point was determined according to a published algorithm.[61] Stiffness was obtained, using the Oliver and Pharr method,[62,63] through the slope of each curve calculated by performing a linear fit to the upper part of the approach force curve (range was selected according to the thickness of the sample and the characteristics of the force distance curves: typically between 3 nN and 5 nN for nanopillars and between 0.1 and 0.5 nN for films). Poisson's ratio was assumed to be 0.5. Image processing was performed using commercial Nanoscope Analysis software (Bruker). Force curve analysis was performed using custom-written Matlab (Mathworks) routines.

Contact angle measurements. Contact angles were measured using a Ramé-Hart contact angle system (Model 290) at different temperatures. In a typical measurement, 1 μL droplet of water at a defined temperature was dispensed onto the surface of the sample. The average contact value was obtained at five different

positions of the same sample. The temperatures of the plate and sample were set to the temperature of each measure. Scheme 2 depicts the sample preparation for determining the contact angle on the surface of the nanopillars. Contact angle measurements have allowed determining the wetting surface properties below and above the LCST using literature values of NIPAm and NIPAm–AAm random copolymers.[64,65] These values were around 31, 37 and 42 °C for 100:0 NIPAm:AAm (PNIPAm$_{100}$), 90:10 NIPAm:AAm (P(NIPAm$_{90}$-co-AAm$_{10}$)) and 80:20 NIPAm:AAm (P(NIPAm$_{80}$-co-AAm$_{20}$)) respectively.

Results and discussion

Sample preparation and characterization

AAO nanoreactors were prepared *via* a two-step electrochemical anodization process in phosphoric acid at a controlled temperature of 0 °C, as described elsewhere.[33] The dimensions of the AAO templates obtained by Scanning Electronic Microscopy (SEM) were 200 nm of pore diameter and ~ 700 nm of pore length. Fig. 1 depicts the SEM images of the nanoreactors obtained.

Thermo-responsive poly(*N*-isopropylacrylamide)-based nano-pillars were synthesized by SI-ATRP on functionalized AAO nanoreactors. In order to tune the LCST, different compositions of NIPAm and AAm were polymerized. For this purpose, Hamner *et al.* proposal was followed, obtaining co-polymer brushes of NIPAm and AAm with a tunable LCST through the incorporation of small amounts of AAm.[64] The LCST value was heightened due to an increase in the hydrophilic characteristics of the system. In the first place, FT-IR spectra were employed at different synthesis steps to monitor the grafting of the ATRP initiator onto the AAO nanoreactor. The ATRP procedure to obtain nanopillars was also monitored by FT-IR and Fig. 2 shows the FT-IR spectra, between 1450 and 4000 cm^{-1}, for the AAO nanoreactor without reactions, the AAO nanoreactor after the silanization procedure and the AAO nanoreactor with the ATRP initiator (α-bromoisobutyryl bromide) and the detailed FT-IR spectra of PNIPAm$_{100}$ close to 2500 and 3200 cm^{-1}.

FT-IR spectra show that the –Br groups have been successfully introduced onto the AAO nanoreactor by silanization and acylation. This methodology was used to characterize the chemical composition of the template along with the grafting of the ATRP initiator procedure. Compared with that of the AAO
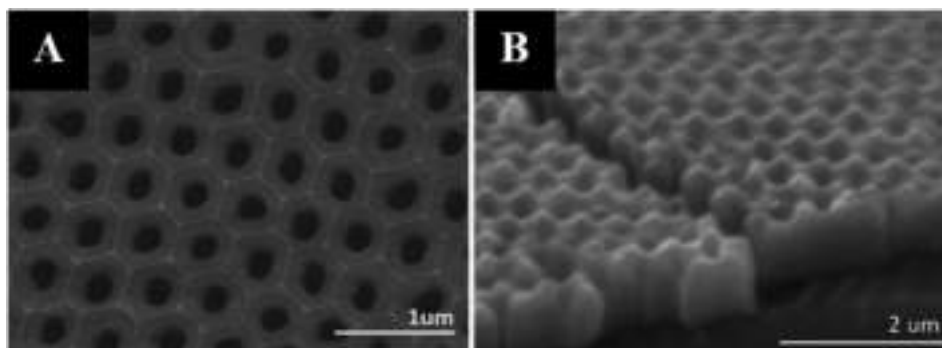
Fig. 1 Morphological characterization of AAO nanoreactors by SEM. The study by SEM allows examining the surface as well as the length of AAO templates. The dimensions of the nanoreactors were ∼200 nm (A) of pore diameter and ∼700 nm of pore length (B).
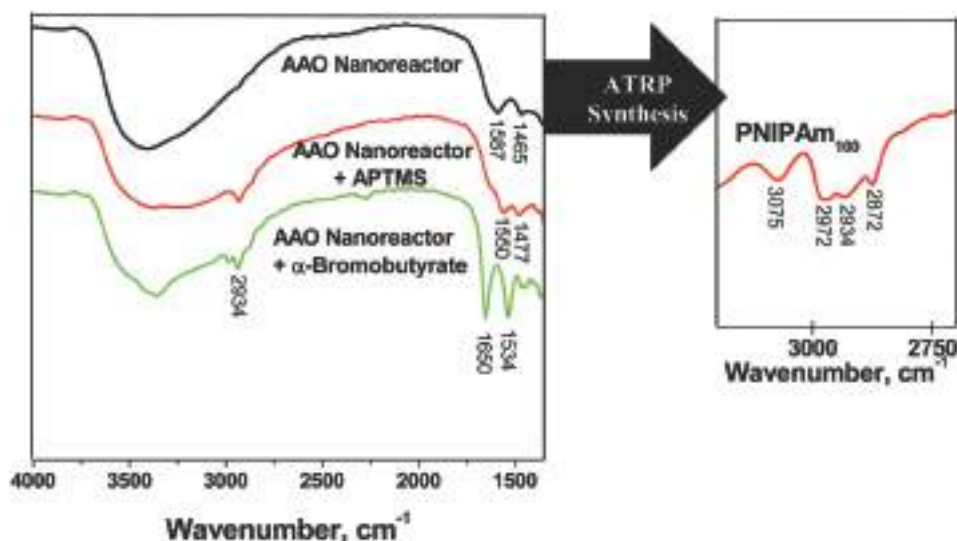

Fig. 2 The FT-IR spectra of AAO membrane, AAO membrane with APTMS and AAO membrane with α-bromoisobutyrate. On the right side, a magnification of PNIPAm$_{100}$ spectra is presented. Below 1450 cm^{-1}, alumina did not allow determining the signals.

nanoreactor, an additional peak of the methylene group (–CH$_2$) appears at 2934 cm^{-1} in the FTIR spectrum of membrane with APTMS. In the spectrum of the AAO template with α-bromo-isobutyrate, the peak of the carbonyl group (C=O) at 1650 cm^{-1} is the characteristic peak of 2-bromoisobutyryl bromide. After the ATRP procedure, the characteristic peaks of PNIPAm, especially the newly emerged methyne (–CH–) and methyl (–CH$_3$) groups at 2972 and 3075 cm^{-1}, indicate that PNIPAm in the AAO nanoreactor has been successfully fabricated by the ATRP method.

Raman spectroscopy was employed to characterize the chemical composition of nanopillars within AAO nanoreactors as previously reported for a similar system.[66] To analyze the presence of the AAm monomer in the PNIPAm nanostructures inside pore nanocavities, the confocal methodology was employed. Fig. 3 illustrates the normalized Raman spectra of PNIPAm$_{100}$, P(NIPAm$_{90}$-co-AAm$_{10}$) and P(NIPAm$_{80}$-co-AAm$_{20}$). The signal at 1650 cm^{-1} corresponding to the carbonyl group present in both monomers and the signal at 2920 cm^{-1} corresponding to the Raman shift of the methyl group present only in the NIPAm[67] monomer allowed examining

qualitatively the change in the nanopillar composition. The I_{CH3}/$I_{C=O}$ ratio was 1.78 for PNIPAM$_{100}$, 1.50 for P(NIPAm$_{90}$-co-AAm$_{10}$) and 1.37 for P(NIPAm$_{80}$-co-AAm$_{20}$), indicating the decrease in the value and an increment of the AAm monomer in the copolymer network.

Unlike the compositional study inside the nanocavity via the confocal approach using Raman spectroscopy, SEM microscopy permitted the evaluation of the morphology of the nanostructures obtained. To this end, the samples were lyophilized before the study in order to preserve morphologies. Fig. 4 provides the details of SEM images for PNIPAm$_{100}$, P(NIPAm$_{90}$-co-AAm$_{10}$) and P(NIPAm$_{80}$-co-AAm$_{20}$).

Fig. 4 confirms that nanopillars were formed through SI-ATRP in the AAO template. Fig. 4 also evidences that the nanopillar sizes are comparable to the size of the AAO nanoreactor.

Mechanical properties

Atomic force microscopy (AFM) has been proved to be a unique tool to probe the nonmechanical properties of hydrogel films.[20,21,68] The mechanical properties of the nanopillars were
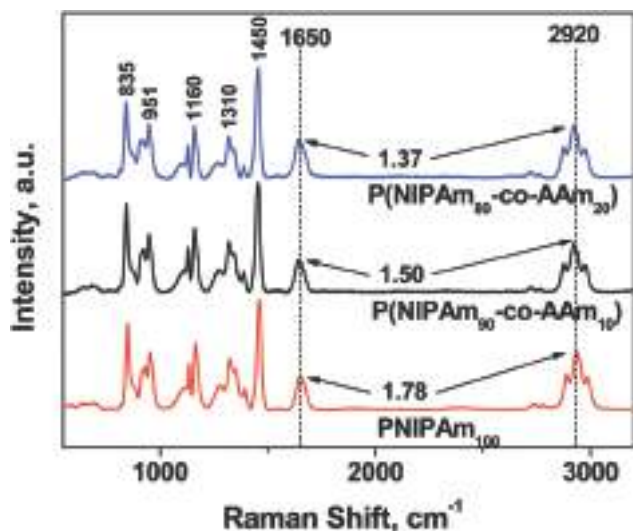
Fig. 3   Raman spectra of PNIPAm$_{100}$, P(NIPAm$_{90}$-co-AAm$_{10}$) and P(NIPAm$_{80}$-co-AAm$_{20}$) and the relationship between the carbonyl group signal at 1650 cm^{-1} present in both monomers and the methyl signal at 2920 cm^{-1} corresponding to the Raman shift of the methyl group present only in the NIPAm monomer.

examined through AFM at different temperatures below and above the LCST. Fig. 5A shows the *in situ* aqueous AFM three-dimensional topography images of PNIPAm$_{100}$ nanopillar surfaces at 27 °C and 35 °C and those of P(NIPAm$_{80}$-co-AAm$_{20}$) nanopillar surfaces at 40 °C and 45 °C. Fig. 5A also presents the representative AFM force–distance curves and the frequency histograms of the Young's modulus of PNIPAm$_{100}$ nanopillars at 27 °C (black) and 35 °C (red) and the same analysis for P(NIPAm$_{80}$-co-AAm$_{20}$) nano-pillars at 40 °C (black) and 45 °C (red). Additionally, Fig. 5B shows the *in situ* aqueous AFM three-dimensional topography images, typical force curves and frequency histograms of the Young's modulus of PNIPAm$_{100}$ hydrogel thin films at 27 °C and 35 °C;

and those of P(NIPAm$_{80}$-co-AAm$_{20}$) hydrogel thin films at 40 °C and 45 °C.

The stiffness of PNIPAm$_{100}$ was shown to increase considerably from approximately 0.9 MPa to 3 MPa as solvent temperature did from 27 to 35 °C. This behavior is in agreement with the chemical rearrangement due to the crosslinked network deswelling as temperature increased the expulsion of solvent. In contrast, the stiffness of P(NIPAm$_{80}$-co-AAm$_{10}$) was shown to decrease considerably from approximately 8.4 to 3.3 MPa when the solvent temperature increased from 40 to 45 °C. According to Xia *et al.*,[1] the Young's modulus increases above the LCST in PNIPAm microgels due to an increment in the density of the polymeric networks. On the other hand, when a hydrophilic monomer was introduced, the behavior of the system changed and the Young's modulus of P(NIPAm$_{80}$-co-AAm$_{20}$) decreased above the LCST. These interesting and novel outcomes suggest that the mechanical properties in the collapsed state of nano-pillars are determined by the thermo-responsive monomer, NIPAm, since the hydrophobic interaction inside the nano-structure produces a packaging thereof, and the values of the Young's modulus above the LCST are the same for both systems, PNIPAm$_{100}$ and P(NIPAm$_{80}$-co-AAm$_{20}$). On the other hand, when the values of the Young's modulus below the LCST were compared, P(NIPAm$_{80}$-co-AAm$_{20}$) resulted an order of magnitude stiffer than PNIPAm$_{100}$. According to Sousaa's explanation,[69] a smaller average free volume radius and size of the AAm monomer permit more effective interaction between the segments in the polymeric network. This results in an increase in polymeric network density, yielding a higher Young's modulus value.

Fig. 5B shows a similar behavior for non-nanostructured PNIPAm$_{100}$ hydrogel thin films. The stiffness of PNIPAm$_{100}$ microgel films was shown to increase considerably from approximately 1.8 MPa to 25.6 MPa as solvent temperature did from 27 to 35 °C. Here, it is possible to see the nanostructure influence in the PNIPAm based microgels: the nanopillars showed a higher soft behavior.
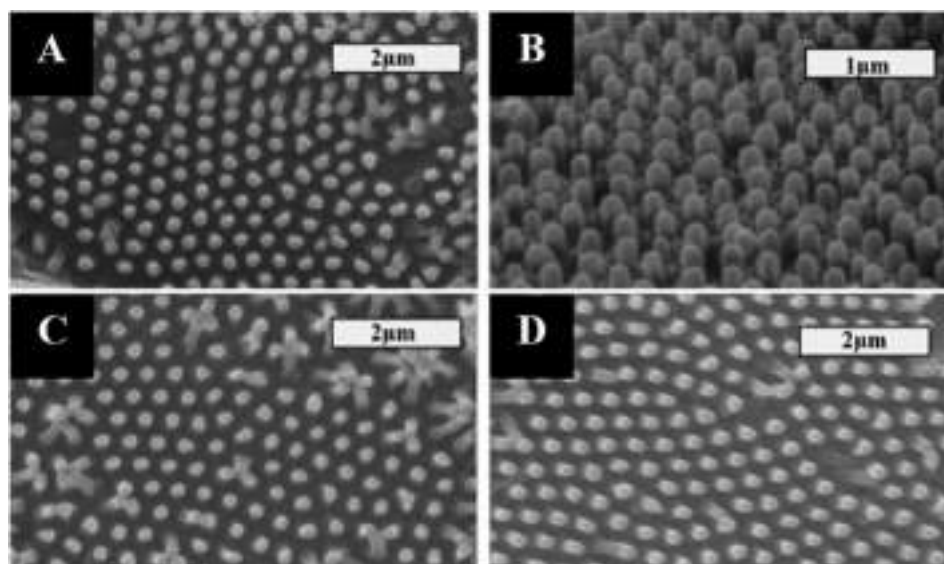

Fig. 4   SEM images of PNIPAm$_{100}$ nanopillars (A) top view, (B) side view, (C) P(NIPAm$_{90}$-co-AAm$_{10}$) and (D) P(NIPAm$_{80}$-co-AAm$_{20}$).
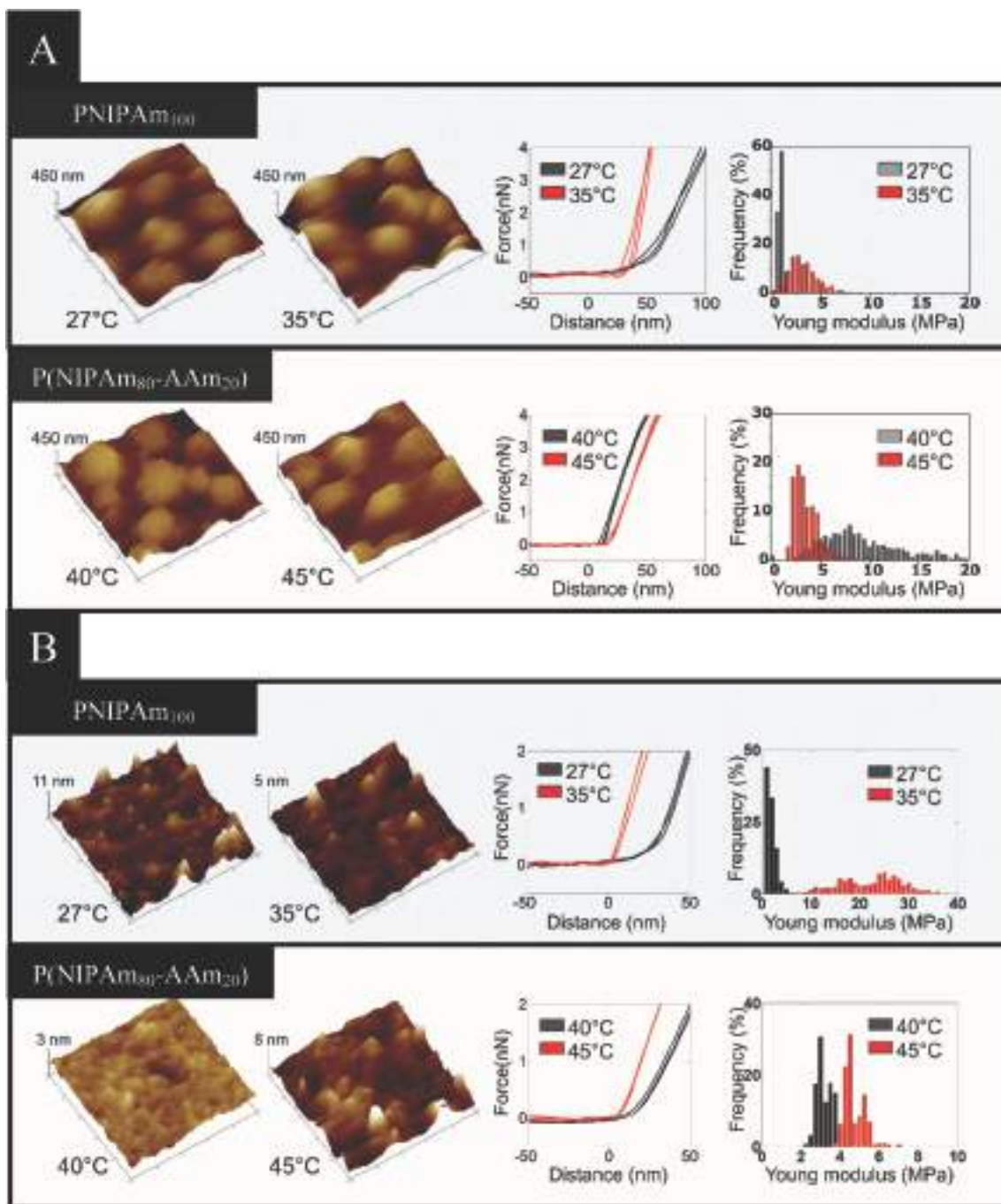
Fig. 5 (A) *In situ* AFM three-dimensional topography images of PNIPAm$_{100}$ nanopillar surfaces at 27 °C and 35 °C, representative force–distance curves and frequency histograms of the Young's modulus of PNIPAm$_{100}$ nanopillars at 27 °C (black, mean stiffness = 0.88 MPa, Std = 0.29 MPa, N = 567 force curves from 7 nanopillars) and at 35 °C (red, mean stiffness = 3.0 MPa, Std = 1.5 MPa, N = 563 force curves from 8 nanopillars). And images of P(NIPAm$_{80}$-*co*-AAm$_{20}$) nanopillar surfaces at 40 °C and 45 °C, force–distance curves and frequency histograms of the Young's modulus of P(NIPAm$_{80}$-*co*-AAm$_{20}$) nanopillars at 40 °C (black, mean stiffness = 8.4 MPa, Std = 11.2 MPa, N = 575 force curves from 11 nanopillars) and at 45 °C (red, mean stiffness = 3.3 MPa, Std = 22.1 MPa, N = 623 force curves from 11 nanopillars). (B) AFM 3D images of PNIPAm$_{100}$ hydrogel film surfaces at 27 °C and 35 °C, representative force–distance curves and frequency histograms of the Young's modulus at 27 °C (black, mean stiffness = 1.8 MPa, Std = 0.9 MPa, N = 590 force curves) and at 35 °C (red, mean stiffness = 25.6 MPa, Std = 12.3 MPa, N = 589 force curves). Images of P(NIPAm$_{80}$-*co*-AAm$_{20}$) hydrogel surfaces at 40 °C and 45 °C, force–distance curves and frequency histograms of the Young's modulus at 40 °C (black, mean stiffness = 3.2 MPa, Std = 0.4 MPa, N = 590 force curves) and at 45 °C (red, mean stiffness = 5.1 MPa, Std = 0.6 MPa, N = 582 force curves). All images were acquired in solution in the PF-QNM mode; scan size: 1 μm × 1 μm, z-scale indicated on each image.

In contrast to the nanostructured system, the stiffness of non-nanostructured P(NIPAm$_{80}$-*co*-AAm$_{20}$) microgels was shown to increase from approximately 3.2 to 5.1 MPa when the solvent temperature increased from 40 to 45 °C. The increment in the stiffness values for non-nanostructured PNIPAm$_{100}$ microgels is considerably higher (14 fold/23.8 MPa) than non-nanostructured

PNIPAm$_{100}$ microgels (1.6 fold/1.9 MPa). In the nanostructured PNIPAm$_{100}$ this effect decreases (3.4 fold/2.1 MPa) and for nanostructured P(NIPAm$_{80}$-co-AAm$_{20}$) the effect is in the opposite direction (2.7 fold decrease/−5.1 MPa), and the material becomes a softer system.

Based on our results, a hypothesis is proposed about hydrophilic surface domains during transition. Specifically, P(NIPAm$_{80}$-co-AAm$_{20}$) could experience a subtle monomer rearrangement during transition. Below the LCST, the nanopillars presented a random distribution of monomers in the polymer network. This distribution provided greater stiffness, due to a more efficient interaction between the segments in the polymer network given the presence of randomly distributed smaller monomers. When the temperature increased above the LCST, the monomer distribution changed; NIPAm monomers concentrated in the center of the nanopillars giving the mechanical properties of NIPAm and the low concentration of AAm monomers was exposed to an aqueous environment. The Young's modulus of P(NIPAm$_{80}$-co-AAm$_{20}$) above the LCST = 3.3 MPa is similar to the Young's modulus of PNIPAm$_{100}$ above the LCST = 3.0 MPa.

Molecular dynamics simulations

To support our hypothesis and understand the possibility that the aggregation of NIPAm segments can occur near the center of the nanopillars displacing locally hydrophilic AAm units towards the surface, we performed Molecular Dynamics (MD) simulations of a cylindrical NIPAm–AAm random copolymer network using Gromacs 4.5.5.[70] This copolymer network had a diamond-like topology.[71] Every crosslinking unit was connected to four random copolymer chains having 100 segments each. All polymer chains were connected to two crosslinks, except those chains that were closer to the cylindrical surface of the nanopillar, which had one of their ends free in solution. Some of these boundary chains were shorter than 100 segments long, such that in the fully extended conformation of the network the radius of the cylinder was 500 nm. The diameter of a segment was 1 nm. In the MD simulations, we imposed a periodic boundary condition in the z-direction. Thus, we modelled a cylindrical nanopillar whose axial length was much larger than its diameter. The network macromolecule was also periodic in the z-direction.

Once the cylindrical polymer network was constructed, each segment, except crosslinks, was randomly labeled as NIPAm or AAm, such that the NIPAm : AAm ratio was 80 : 20%. This ratio applies to the whole network, even though it may differ for individual chains. As a result, the simulated system contained 113 crosslinks, 4621 AAm units, and 18 483 NIPAm segments. We also performed MD simulations where all units, except crosslinks, were NIPAm.

The force field used in these MD simulations had been previously described.[72,73] Bonded units interacted with a finite extensible nonlinear elastic (FENE) potential

$$U_{\text{FENE}}(r_{ij}) = \begin{cases} -\dfrac{k}{2}R_0^2 \ln\left(1 - \dfrac{r_{ij}^2}{R_0^2}\right) & r_{ij} \leq R_0 \\ \infty & r_{ij} > R_0 \end{cases}$$

where r_{ij} is the distance between bonded segments i and j. Non-bonded AAm units interact with a repulsive (shifted) Lennard-Jones potential:

$$U_{\text{RP}}(r_{ij}) = \begin{cases} 4\varepsilon\left[\left(\dfrac{\sigma}{r_{ij}}\right)^{12} - \left(\dfrac{\sigma}{r_{ij}}\right)^6 + \dfrac{1}{4}\right] & r_{ij} \leq 2^{1/6}\sigma \\ 0 & r_{ij} > 2^{1/6}\sigma \end{cases}$$

In this case, r_{ij} is the distance between non-bonded segments i and j. Non-bonded NIPAm–AAm interactions are also described with U_{RP}. If the temperature is below its LCST, non-bonded NIPAm segments also interact with this repulsive potential. In contrast, for temperatures above the LCST, NIPAm units become hydrophobic. To describe this behavior these segments interact with a Lennard-Jones potential, where ε is the well depth:

$$U_{\text{attr}}(r_{ij}) = 4\varepsilon\left[\left(\dfrac{\sigma}{r_{ij}}\right)^{12} - \left(\dfrac{\sigma}{r_{ij}}\right)^6\right]$$

In this work, we used $\varepsilon = k_{\text{B}}T$, where T is the temperature, and $\sigma = 1$ nm, $R_0 = 1.5\sigma$ and $k = 30\dfrac{\varepsilon}{\sigma^2}$ to avoid bond crossing.

We considered three different temperatures, including situations below (T_1) and above (T_2 and T_3; $T_3 > T_2$) the LCST of NIPAm. For each temperature, 10 ns long (after equilibration) NVT MD simulations were performed using a Berendsen thermostat and a 1 fs timestep. For non-bonded interactions, a spherical cutoff of 2σ was applied.

Fig. 6 displays typical network conformations of NIPAm and NIPAm–AAm nanopillars at each of the temperatures considered. While the pure NIPAm structure collapses at $T_2 >$ LCST, the collapse of the copolymer nanopillar requires a higher temperature, $T_3 > T_2$. Thus, as observed in our experiments, the presence of the AAm co-monomer increases the collapse temperature of the nanopillar, with respect to that of a pure NIPAm network.

To quantify this behavior, the local (total) polymer distribution $\rho_{\text{p}}(r)$ was used. It measures the average number of network segments (including crosslinks and NIPAm and AAm units) contained in a volume element at a distance r from the nanopillar center of mass. This density was calculated constructing a histogram using 10 000 time steps of our MD simulations. Using this polymer density, the radius of the nanopillar, R_{NP}, can be defined as twice the first moment distribution:

$$R_{\text{NP}} = \frac{\int_0^\infty r\rho_{\text{p}}(r)(2r)\,\mathrm{d}r}{\int_0^\infty r\rho_{\text{p}}(r)\,\mathrm{d}r}$$

Fig. 7A shows $2\pi r\rho_{\text{p}}(r)$ for PNIPAm$_{100}$ and P(NIPAm$_{80}$-co-AAm$_{20}$) nanopillars at the different temperatures considered. Note that the area under these curves must be identical, since

$$N_{\text{p}} = \int_0^\infty 2\pi r\rho_{\text{p}}(r)\,\mathrm{d}r$$

where N_{p} is the average number of segments per unit of axial length. Below PNIPAm$_{100}$ LCST (T_1), both nanopillars showed a wide polymer distribution that extended for several nanometers ($R_{\text{NP}} = 55$ nm), which indicates a water-soluble network. At temperature $T_2 >$ LCST, pure PNIPAm$_{100}$ nanopillars showed
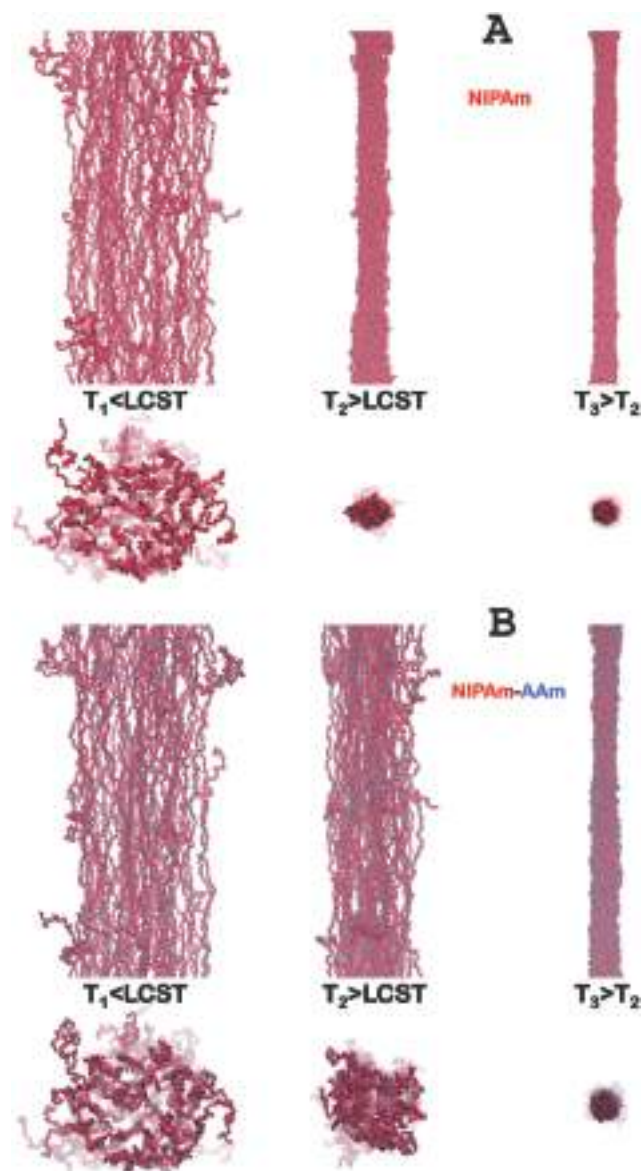
Fig. 6 Scheme showing the side (above) and top (below) views of typical network conformations resulting from our MD simulations at different temperatures of NIPAm (A) and NIPAm–AAm (B) nanopillars. Blue spheres correspond to AAm units and red spheres represent NIPAm segments.

Fig. 7 (A) Plot of the total density of the polymer, $\rho_p(r)$, as a function of the distance from the center of the nanopillar, r, for both NIPAm–AAm (solid lines) and pure NIPAm (dashed lines) nanopillars. At T_1, both networks present identical total density profiles. (B) AAm (blue) and NIPAm (red) local density profiles for copolymer nanopillars below the LCST (T_1, solid lines) and above the collapse temperature (T_3, dashed lines).

a narrow polymer distribution with $R_{NP} = 12$ nm, where most of the polymer was contained within few nanometers (see Fig. 7A), which is a sign of a collapsed network. Conversely, the P(NIPAm$_{80}$-co-AAm$_{20}$) nanopillar featured a wider polymer distribution with $R_{NP} = 36$ nm, which implies that this structure is soluble at this temperature. To observe the collapse of the NIPAm–AAm structure ($R_{NP} = 10$ nm), a temperature T_3 higher than T_2 is required. The pure PNIPAm network also collapsed at this higher temperature ($R_{NP} = 9$ nm).

The NIPAm–AAm network collapsed when temperature increased due to the aggregation of hydrophobic units. The main goal of our MD simulations was to show that NIPAm se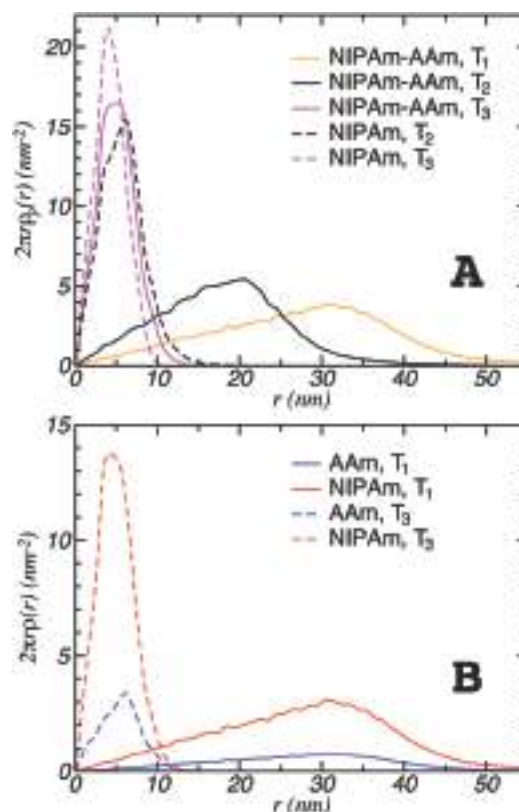gment aggregation displaced hydrophilic units towards the surface. To quantify the excess fraction of AAm units near the surface, we defined

$$f_{AAm} = \frac{\int_{R_{NP}-\delta_p}^{\infty} r \rho_{AAm}(r)\,dr}{\int_{R_{NP}-\delta_p}^{\infty} r(\rho_{AAm}(r) + \rho_{NIPAm}(r))\,dr}$$

where $\rho_{AAm}(r)$ and $\rho_{NIPAm}(r)$ are the local distributions of AAm and NIPAm units, respectively, and δ_p is a penetration depth that measures the length of the water–nanopillar interface.

In our MD simulations, $f_{AAm} = 0.12$ was calculated when $T = T_1$, $f_{AAm} = 0.27$ when $T = T_2$ and $f_{AAm} = 0.33$ when $T = T_3$ using $\delta_p = 5$ nm (a similar trend can be obtained using $\delta_p = 2$ and 10 nm). Thus, as temperature increased above the LCST, we predicted a higher concentration of hydrophilic units near the surface. Thus, as P(NIPAm$_{80}$-co-AAm$_{20}$) nanopillars collapsed when the temperature increased, a higher concentration of hydrophilic units was predicted near the surface.

Water contact angle measurements

According to the higher concentration of hydrophilic units near the surface, nano-structured hydrogels were prepared with tunable wettability properties through the introduction of a hydrophilic monomer. In order to analyze this proposal, the nanopillar
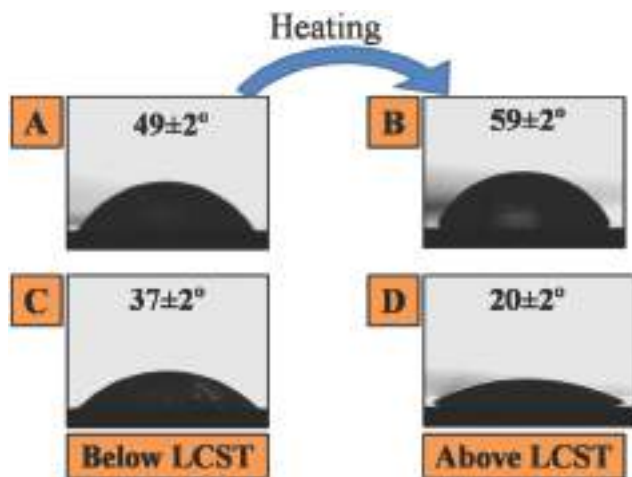
Fig. 8 Contact angle pictures of PNIPAm$_{100}$ (A and B, 27 and 35 °C respectively) and P(NIPAm$_{80}$-co-AAm$_{20}$) (C and D, 40 and 45 °C respectively) nanopillars below and above the LCST. The nanopillars were supported on glass.

properties on the surface were evaluated by water contact angle measurements at different temperatures (Fig. 8).

Fig. 8 displays the variation of the contact angles as a function of the monomer composition of the nanopillars and temperature. For PNIPAm$_{100}$, the behavior shows an increment in the hydrophobicity surface when temperature is increased, from Fig. 8A to B. In contrast, P(NIPAm$_{80}$-co-AAm$_{20}$) maintains the opposite behavior, the hydrophilicity surface increases as temperature does from Fig. 8C to D.

In order to evaluate the potential wettability of the nano-structures, the contact angles over PNIPAm$_{100}$ and P(NIPAm$_{80}$-co-AAm$_{20}$) hydrogel thin films obtained by surface-initiated atom-transfer radical polymerization from glass were evaluated. Fig. 9 illustrates the higher values of contact angles for all cases of
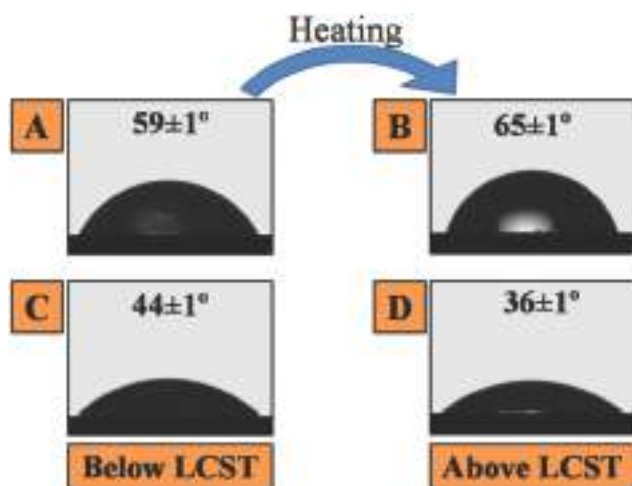

Fig. 9 Contact angle pictures of PNIPAm$_{100}$ (A and B, 27 and 35 °C respectively) and P(NIPAm$_{80}$-co-AAm$_{20}$) (C and D, 40 and 45 °C respectively) hydrogel thin films below and above the LCST. The hydrogel thin films were obtained by surface-initiated atom-transfer radical polymerization from glass.

hydrogel thin films, demonstrating the interpenetration effect in the nanostructured films. Moreover due to the accumulation of AAm monomers on the surface and the interpenetration effect, the $\Delta\theta$ values for P(NIPAm$_{80}$-co-AAm$_{20}$) nanopillars was higher than those for P(NIPAm$_{80}$-co-AAm$_{20}$) thin films.

Several systems based on PNIPAm hydrogels have been used as biomedical devices. An important parameter to define a biomaterial is its interaction with water on the surface. As a consequence, it is central to understand and characterize water uptake by our nanopillars. Ko et al. designed thermo-responsive chemical connectors based on hybrid nanowires.[74] NIPAm presence in these materials provided thermally tunable surface wetting properties and the transition of the water contact angle showed important changes below and above the LCST of NIPAm. This result allowed the authors to design programmable fasteners based on hybrid nanowires that reversibly change their wet adhesion strength by around 170 times in response to a thermo-responsive interpreter. On the other hand, Yang et al.[75] reported the development of a thermo-responsive block copolymer based on PNIPAm as a switch for controllable water transportation through AAO membrane.

Considering that the application of 5 nN in the AFM measurement gives information about the mechanical properties between 50 and 110 nm inside the nanopillar (taking into account the spring constants of the AFM probes used) and that contact angle measurements do so up to 10 nm, we evaluated the surface properties by contact angle measurement and the properties within the material by AFM. Our nanopillars presented a peculiar and interesting behavior. Contrary to the results obtained by AFM, which suggest that the mechanical properties inside the nanopillars were determined by the thermo-responsive monomer, NIPAm, the water contact angle over the nanopillars surface was determined by the non-thermoresponsive monomer, AAm (hydrophilic monomer). These results give information about the spatial distribution of monomer units in the nanopillar structure below and above the LCST. Specifically, P(NIPAm$_{80}$-co-AAm$_{20}$) could experience a monomer rearrangement during transition. Below the LCST, nanopillars presented a random distribution of monomers in the polymer network. This distribution, not only provides a more hydrophilic character to nanopillars with respect to NIPAm nanopillars, but also greater stiffness, due to a more effective interaction between the segments in the polymer network given the presence of smaller monomers being randomly distributed. When temperature increased above the LCST, the monomer distribution changed; NIPAm monomers concentrated in the center of nanopillars, imparting the mechanical properties of NIPAm and AAm monomers were exposed to an aqueous environment, leading to higher affinity to water.

Conclusion

A promising nanomaterial based on poly N-isopropylacrylamide nanopillars with thermally-induced softening was designed and prepared through surface initiation atom-transfer radical polymerization in synthesized anodized aluminum oxide templates.

The introduction of a more hydrophilic co-monomer, acrylamide, in the nanostructures obtained produced an interesting change in their mechanical properties and provided a strategy to tune these features. When temperature was increased above the LCST, the stiffness of PNIPAm nanopillars increased as well, as opposed to the stiffness of PNIPAm–AAm nanopillars that decreased. Based on this behavior, we formulated a hypothesis: a possible local molecular rearrangement in our nanosystems at the LCST. Below the LCST, the copolymer nanopillars presented a random distribution of monomers in the polymer network but, when temperature increased, the aggregation of NIPAm segments occurred near the center of the nanopillars displacing hydrophilic AAm units towards the surface.

The molecular dynamics simulations performed described the increase of the nanostructure's LCST. These results supported the hypothesis proposed that as temperature increases above the LCST a higher concentration of hydrophilic units near the surface results in enhanced hydrophilicity.

Finally, the determination of the contact angles below and above the LCST allowed confirming the presence of AAm units towards the surface due to an increment in the wettability after transition in the nanopillars with the hydrophilic monomer.

We believe that the novel and interesting system shown by PNIPAM-based nanopillars could have strong implications for the use and application of thermo-responsive surfaces in multiple fields. Moreover, it could be especially important for the molecular design of polymer-based vehicles for tissue engineering, drug delivery, and regenerative medicine among others.

Acknowledgements

References

1 L.-W. Xia, R. Xie, X.-J. Ju, W. Wang, Q. Chen and L.-Y. Chu, *Nat. Commun.*, 2013, **4**, 2226.

2 J. S. Kahn, A. Trifonov, A. Cecconello, W. Guo, C. Fan and I. Willner, *Nano Lett.*, 2015, **15**(11), 7773–7778.

3 A. Sidorenko, T. Krupenkin, A. Taylor, P. Fratzl and J. Aizenberg, *Science*, 2007, **315**(5811), 487–490.

4 L. V. Sigolaeva, S. Y. Gladyr, A. P. H. Gelissen, O. Mergel, D. V. Pergushov, I. N. Kurochkin, F. A. Plamper and W. Richtering, *Biomacromolecules*, 2014, **15**(10), 3735–3745.

5 M. C. LeMieux, S. Peleshanko, K. D. Anderson and V. V. Tsukruk, *Langmuir*, 2007, **23**(1), 265–273.

6 J. P. Best, M. P. Neubauer, S. Javed, H. H. Dam, A. Fery and F. Caruso, *Langmuir*, 2013, **29**(31), 9814–9823.

7 P. C. Georges and P. a. Janmey, *J. Appl. Physiol.*, 2005, **98**(4), 1547–1553.

8 J. P. Best, S. Javed, J. J. Richardson, K. L. Cho, M. M. J. Kamphuis and F. Caruso, *Soft Matter*, 2013, **9**(18), 4580.

9 M. Kaholek, W. K. Lee, J. Feng, B. Lamattina, D. J. Dyer and S. Zauscher, *Chem. Mater.*, 2006, **18**(16), 3660–3664.

10 J. Peng, T. Qi, J. Liao, M. Fan, F. Luo, H. Li and Z. Qian, *Nanoscale*, 2012, **4**(8), 2694.

11 J. a. Yang, J. Yeom, B. W. Hwang, A. S. Hoffman and S. K. Hahn, *Prog. Polym. Sci.*, 2014, 1–14.

12 L. Ionov, *Mater. Today*, 2014, **17**(10), 494–503.

13 D. Wang, D. Cheng, Y. Guan and Y. Zhang, *Biomacromolecules*, 2011, **12**(3), 578–584.

14 J. Shen, T. Ye, A. Chang, W. Wu and S. Zhou, *Soft Matter*, 2012, 12034–12042.

15 M. Molina, M. Asadian-Birjand, J. Balach, J. Bergueiro, E. Miceli and M. Calderón, *Chem. Soc. Rev.*, 2015, **44**, 6161–6186.

16 P. A. L. Fernandes, S. Schmidt, M. Zeiser, A. Fery and T. Hellweg, *Soft Matter*, 2010, **6**(15), 3455–3458.

17 B. S. Forney, C. Baguenard and C. A. Guymon, *Soft Matter*, 2013, **9**(31), 7458–7467.

18 Y. Kaneko, S. Nakamura, K. Sakai, A. Kikuchi, T. Aoyagi, Y. Sakurai and T. Okano, *J. Biomater. Sci., Polym. Ed.*, 1999, **10**(11), 1079–1091.

19 D. Schmaljohann, J. Oswald, B. Jørgensen, M. Nitschke, D. Beyerlein and C. Werner, *Biomacromolecules*, 2003, **4**(6), 1733–1739.

20 X. Cheng, H. E. Canavan, M. J. Stein, J. R. Hull, S. J. Kweskin, M. S. Wagner, G. a. Somorjai, D. G. Castner and B. D. Ratner, *Langmuir*, 2005, **21**(17), 7833–7841.

21 S. Schmidt, M. Zeiser, T. Hellweg, C. Duschl, A. Fery and H. Möhwald, *Adv. Funct. Mater.*, 2010, **20**(19), 3235–3243.

22 S. M. Hashmi and E. R. Dufresne, *Soft Matter*, 2009, **5**(19), 3682–3688.

23 K. Na, J. H. Park, S. W. Kim, B. K. Sun, D. G. Woo, H.-M. Chung and K.-H. Park, *Biomaterials*, 2006, **27**(35), 5951–5957.

24 Y. H. Bae, B. Vernon, C. K. Han and S. W. Kim, *J. Controlled Release*, 1998, **53**(1–3), 249–258.

25 J. Virtanen and H. Tenhu, *Macromolecules*, 2000, **33**(16), 5970–5975.

26 H. Yoshioka, M. Mikami, Y. Mori and T. Eishun, *J. Macromol. Sci., Part A: Pure Appl. Chem.*, 1994, **31**(1), 113–120.

27 I. V. Berlinova, I. V. Dimitrov, N. G. Vladimirov, V. Samichkov and Y. Ivanov, *Polymer*, 2001, **42**(14), 5963–5971.

28 D. Singh, D. Kuckling, V. Koul, V. Choudhary, H. J. Adler and A. K. Dinda, *Eur. Polym. J.*, 2008, **44**(9), 2962–2970.

29 W. Liu, B. Zhang, W. W. Lu, X. Li, D. Zhu, K. De Yao, Q. Wang, C. Zhao and C. Wang, *Biomaterials*, 2004, **25**(15), 3005–3012.

30 X. Z. Zhang and C. C. Chu, *J. Mater. Sci.: Mater. Med.*, 2007, **18**(9), 1771–1779.

31 J. F. Pollock and K. E. Healy, *Acta Biomater.*, 2010, **6**(4), 1307–1318.

32 L. Janovák, J. Varga, L. Kemény and I. Dékány, *Colloid Polym. Sci.*, 2008, **286**(14–15), 1575–1585.

33 J. Martín, J. Maiz, J. Sacristan and C. Mijangos, *Polymer*, 2012, **53**(6), 1149–1166.

34 L. Noirez, C. Stillings, J.-F. Bardeau, M. Steinhart, S. Schlitt, J. H. Wendorff and G. Pépy, *Macromolecules*, 2013, **46**(12), 4932–4936.

35 W. Knoll, A.-M. Caminade, K. Char, H. Duran, C. L. Feng, A. Gitsas, D. H. Kim, A. Lau, T. D. Lazzara, J.-P. Majoral, M. Steinhart, B. Yameen and X. H. Zhong, *Small*, 2011, **7**(10), 1384–1391.

36 B. Pulamagatta, M. Y. E. Yau, I. Gunkel, T. Thurn-Albrecht, K. Schröter, D. Pfefferkorn, J. Kressler, M. Steinhart and W. H. Binder, *Adv. Mater.*, 2011, **23**(6), 781–786.

37 J. L. Perry, P. Guo, S. K. Johnson, H. Mukaibo, J. D. Stewart and C. R. Martin, *Nanomedicine*, 2010, **5**(8), 1151–1160.

38 J. M. Giussi, I. Blaszczyk-Lezak, B. Sanz, P. E. Allegretti, C. Mijangos and M. S. Cortizo, *Eur. Polym. J.*, 2014, **59**, 84–93.

39 X. Sheng and J. Zhang, *Langmuir*, 2009, **25**(12), 6916–6922.

40 H. Duran, M. Steinhart, H.-J. Butt and G. Floudas, *Nano Lett.*, 2011, **11**(4), 1671–1675.

41 R. M. Michell, A. T. Lorenzo, A. J. Müller, M.-C. Lin, H.-L. Chen, I. Blaszczyk-Lezak, J. Martín and C. Mijangos, *Macromolecules*, 2012, **45**(3), 1517–1528.

42 I. Blaszczyk-Lezak, J. Maiz, J. Sacristán and C. Mijangos, *Ind. Eng. Chem. Res.*, 2011, **50**(18), 10883–10888.

43 J. M. Giussi, I. Blaszczyk-Lezak, M. S. Cortizo and C. Mijangos, *Polymer*, 2013, **54**(26), 6886–6893.

44 M. Salsamendi, N. Ballard, B. Sanz, J. M. Asua and C. Mijangos, *RSC Adv.*, 2015, **5**(25), 19220–19228.

45 B. S. a. Sapp and B. B. Lakshmi, *Adv. Mater.*, 1999, **11**(5), 402–404.

46 C.-W. Chang, M.-H. Chi, C.-W. Chu, H.-W. Ko, Y.-H. Tu, C.-C. Tsai and J.-T. Chen, *RSC Adv.*, 2015, **5**(35), 27443–27448.

47 H. J. Wang, W. H. Zhou, X. F. Yin, Z. X. Zhuang, H. H. Yang and X. R. Wang, *J. Am. Chem. Soc.*, 2006, **128**(50), 15954–15955.

48 W.-C. Wang, J. Wang, Y. Liao, L. Zhang, B. Cao, G. Song and X. She, *J. Appl. Polym. Sci.*, 2010, **117**(1), 534–541.

49 R. Barbey, L. Lavanant, D. Paripovic, N. Schüwer, C. Sugnaux, S. Tugulu and H.-A. Klok, *Chem. Rev.*, 2009, **109**(11), 5437–5527.

50 Q. Li and L. Tang, *J. Polym. Sci., Part A: Polym. Chem.*, 2014, **52**(13), 1862–1868.

51 Q. Li, L.-M. Tang and Y. Jiao, *Acta Polym. Sin.*, 2014, (8), 1135–1142.

52 Q. Li, L.-M. Tang and Y. Liang, *Gaodeng Xuexiao Huaxue Xuebao/Chem. J. Chin. Univ.*, 2013, **34**(6), 1542–1546.

53 Q. Li, L. Tang, Y. Xia and B. Li, *Macromol. Rapid Commun.*, 2013, **34**(2), 185–189.

54 A. M. Md Jani, D. Losic and N. H. Voelcker, *Prog. Mater. Sci.*, 2013, **58**(5), 636–704.

55 H. Seto, M. Takara, C. Yamashita, T. Murakami, T. Hasegawa, Y. Hoshino and Y. Miura, *ACS Appl. Mater. Interfaces*, 2012, **4**(10), 5125–5133.

56 J. Wang, J. Dai, M. Meng, Z. Song, J. Pan, Y. Yan and C. Li, *J. Appl. Polym. Sci.*, 2014, **131**, 40310.

57 Y. Cui, C. Tao, S. Zheng, Q. He, S. Ai and J. Li, *Macromol. Rapid Commun.*, 2005, **26**(19), 1552–1556.

58 P. F. Li, R. Xie, J. C. Jiang, T. Meng, M. Yang, X. J. Ju, L. Yang and L. Y. Chu, *J. Membr. Sci.*, 2009, **337**(1–2), 310–317.

59 M. Wei, Y. Gao and M. J. Serpe, *J. Mater. Chem. B*, 2015, **3**, 744–747.

60 J. L. Hutter and J. Bechhoefer, *Rev. Sci. Instrum.*, 1998, **64**, 1868.

61 D. C. Lin, E. K. Dimitriadis and F. Horkay, *J. Biomech. Eng.*, 2007, **129**(6), 904–912.

62 W. C. Oliver and G. M. Pharr, *J. Mater. Res.*, 1992, **7**(6), 1564–1580.

63 M. Plodinec, M. Loparic, C. A. Monnier, E. C. Obermann, R. Zanetti-Dallenbach, P. Oertle, J. T. Hyotyla, U. Aebi, M. Bentires-Alj, R. Y. H. Lim and C.-A. Schoenenberger, *Nat. Nanotechnol.*, 2012, **7**(11), 757–765.

64 K. L. Hamner and M. M. Maye, *Langmuir*, 2013, **29**, 15217–15223.

65 K. L. Hamner, C. M. Alexander, K. Coopersmith, D. Reishofer, C. Provenza and M. M. Maye, *ACS Nano*, 2013, **7**(8), 7011–7020.

66 J. M. Giussi, I. Blaszczyk-Lezak, P. E. Allegretti, M. S. Cortizo and C. Mijangos, *Polymer*, 2013, **54**(18), 5050–5057.

67 H. Yamauchi and Y. Maeda, *J. Phys. Chem. B*, 2007, **111**(45), 12964–12968.

68 A. Burmistrova, M. Richter, M. Eisele, C. Üzüm and R. von Klitzing, *Polymers*, 2011, **3**(4), 1575–1590.

69 R. G. Sousaa, R. F. S. Freitas and M. F. Welington, *Polymer*, 1998, **39**(16), 3815–3819.

70 B. Hess, C. Kutzner, D. Van Der Spoel and E. Lindahl, *J. Chem. Theory Comput.*, 2008, **4**(3), 435–447.

71 M. Quesada-Pérez, J. Ramos, J. Forcada and A. Martín-Molina, *J. Chem. Phys.*, 2012, **136**, 244903.

72 K. Kremer and G. S. Grest, *J. Chem. Phys.*, 1990, **92**(8), 5057.

73 G. S. Longo, M. Olvera, D. Cruz and I. Szleifer, *ACS Nano*, 2013, **7**, 2693–2704.

74 H. Ko, Z. Zhang, Y. L. Chueh, E. Saiz and A. Javey, *Angew. Chem., Int. Ed.*, 2010, **49**(3), 616–619.

75 J. Yang, M. Hida, S. Mao, H. Zeng, H. Nakajima and K. Uchiyama, *Chem. Commun.*, 2014, **50**, 10265–10268.